Inverting for dynamic stress evolution on earthquake faults directly from seismic recordings

Qingjun Meng[1], Benchun Duan[1], Dunyu Liu[2], Yongen Cai[3]

[1]Department of Geology & Geophysics, Texas A&M University

[2]Institute for Geophysics, University of Texas, Austin

[3]Institute of Theoretical and Applied Geophysics, Peking University

Key points

- We develop a fault-stress model of earthquake sources that provides a new paradigm comparing with the kinematic slip model.
- We present an inversion method based on the fault-stress model to invert for dynamic stress evolution directly from seismic data.
- Tests on a synthetic model, a checkerboard model and the 2016 Cushing earthquake show the dynamic stress inversion method works well.

Abstract

Dynamic stress evolution during earthquake rupture contains information of fault frictional behavior that governs dynamic rupture propagation. Most of earthquake stress drop and evolution studies are based on kinematic slip inversions. Several dynamic inversion methods in the literature require dynamic rupture modeling that makes them cumbersome with limited applicability. In this study, we develop a fault-stress model of earthquake sources in the framework of the representation theorem. We then propose a dynamic stress inversion method based on the fault-stress model to directly invert for dynamic stress evolution process on the fault plane by fitting seismic data. In this inversion method, we calculate numerical Green's function once only, using an explicit finite element method *EQdyna* with a unit change of shear or normal stress on each subfault patch. A linear least-squares procedure is used to invert for stress evolution history on the fault. To stabilize the inversion process, we apply several constraints including zero normal slip (no separation or penetration of the fault), non-negative shear slip, and moment constraint. The method performs well and reliably on a synthetic model, a checkerboard model and the 2016 M_w 5.0 Cushing (Oklahoma) earthquake. The proposed fault-stress model of earthquake sources with inversion techniques such as one presented in this study provides a new paradigm for earthquake source studies using seismic data, with a potential of deciphering more physics from seismic recordings of earthquakes.

Plain Language Summary

Scientists have been fitting seismic recordings to obtain slip (relative motion between two sides of a geology fault that causes earthquakes) and slip evolution to understand what

happen during an earthquake. This is the fault-slip (or kinematic) model of earthquake sources that have been in dominance in the literature and scientific community. To understand why earthquakes happen in ways observed in past earthquakes, scientists further calculate stress changes and stress evolution, which control earthquake rupture processes, from the above slip distribution and slip evolution with some assumptions. In this study, we propose a fault-stress model of earthquake sources and present an inversion method based on this model to directly obtain stress change and evolution during an earthquake from seismic recordings. Tests on a couple of hypothetical models and the 2016 Mw 5.0 Cushing (Oklahoma) earthquake show the fault-stress model and the inversion method perform well. The proposed fault-stress model with inversion techniques such as one presented in this study provides a new paradigm for scientists to study earthquake sources from seismic recordings, potentially advancing our understanding of earthquake physics and improving our ability for seismic hazard analysis and reduction greatly.

Index terms: 7209, 7215, 7260, 7290

Keywords: dynamic inversion, fault-stress model, least-squares method, Green's function, earthquake source, seismic recordings

1. Introduction

Kinematic slip inversions have been the primary approach for the scientific community to understand sources of earthquakes, such as the 1979 Mw 6.5 Imperial Valley (California) (Olson and Apsel, 1982; Hartzell and Heaton, 1983), 1984 Mw 6.2 Morgan Hill (California)

(Hartzell and Heaton, 1986; Beroza and Spudich, 1988), 1992 Mw 7.3 Landers (California) (Wald and Heaton, 1994; Wang et al., 2022), 1999 Mw 7.6 Chi-Chi (Taiwan) (Ma et al., 2000; Ji et al., 2003), 2004 Mw 9.1 Sumatra (Indonesia) (Ammon et al., 2005; Yoshimoto and Yamanaka, 2014), 2011 Mw 9.0 Tohoku (Japan) (Yue and Lay, 2011; Yamazaki et al., 2011), and 2016 Mw 7.8 Kaikoura (New Zealand) (Zhang et al., 2017; Wang et al., 2018) earthquakes, among many others. By inverting seismic and/or geodetic data, one can obtain slip distribution and/or spatiotemporal slip evolution on the causal fault of an earthquake. Slip distribution shows where and how much slip occurs on the fault in an earthquake. Spatiotemporal slip evolution reveals how rupture propagates along the fault, such as rupture velocity, direction, and slip rise time. These results from slip inversions have provided majority of understanding of past earthquakes from a kinematic point of view.

To gain further knowledge of physics of earthquake sources from earthquakes, several lines of efforts have been made in the literature to obtain dynamic parameters and/or models of past earthquakes. One line of efforts is to obtain static stress changes from slip distributions. Andrews (1980) developed a formulation that relates the slip-parallel shear stress change to the slip distribution in the wavenumber domain. Ripperger and Mai (2004) extended Andrews' formation for fast computation of the shear stress drop distribution on a fault from the slip distribution of a kinematic inversion. This method has been used in other studies. For example, Luttrel et al. (2011) estimated the coseismic stress drop from the slip distribution of the 2010 Mw 8.8 Maule (Chile) earthquake using the method. Okada (1992)'s analytical expressions allow one to calculate static stress (tensor) changes in an elastic homogeneous half space from a given final fault slip distribution. The analytical solutions have been adopted in widely used Coulomb stress change calculations (King et

al., 1994; Lin and Stein, 2004). One limitation of these methods in calculating either static shear stress drops or static stress tensor changes from slip distributions is that the fault is assumed to be embedded in a homogeneous medium. In addition, Ripperger and Mai's method and Andrews's formulation further assumes the fault is embedded in a full space. In addition, the accuracy of these static stress calculations is strongly dependent on the quality of kinematic slip inversion results.

The second line of efforts is to compute dynamic stress changes (i.e., stress evolution during the coseismic dynamic rupture process) of an earthquake from its kinematically-determined spatiotemporal slip evolution. Quin (1990) used a trial-and-error method to obtain a dynamic rupture model to fit the kinematic inversion results of the 1979 Imperial Valley earthquake. Miyatake (1992) proposed a similar method to reconstruct dynamic rupture process of an earthquake from kinematic constraints. In both studies, the frictional coefficient is assumed to drop from the static level to the dynamic level instantaneously at failure, which results in nonphysical stress and slip-rate singularities at the crack tip. In addition, they did not calculate the theoretical waveforms based on their dynamic rupture parameters, which makes it difficult to evaluate the degree of fit of these dynamic models to the recorded seismograms. Fukuyama and Mikumo (1993) developed an iterative method of a kinematic slip inversion and a crack inversion to estimate dynamic rupture properties of an earthquake, including dynamic stress drop and shear strength excess, by fitting near-field seismograms. Bouchon (1997) developed an approach to directly derive the spatiotemporal stress evolution on the fault from the kinematic slip evolution of an earthquake, by using the expressions linking the P-wave scalar potential and S-wave vector potential in the medium with the seismic moments of the fault points. The method was used

111 to compute stress drop (both static and dynamic) and strength excess distributions on the
112 faults for the 1979 Imperial Valley, 1984 Morgan Hill, 1989 Loma Prieta, and 1994
113 Northridge earthquakes (all in California) (Bouchon, 1997), to gain insights into the state
114 of stress before the earthquakes and heterogeneous distributions of stress drop and strength
115 excess. The method was also used to study the complex rupture in the 1992 Landers
116 (California) earthquake, revealing the important role of large dynamic stress perturbations
117 in the earthquake (Bouchon et al., 1998). Ide and Takeo (1997) proposed to solve
118 elastodynamic equations with a finite difference method to determine fault stress evolution
119 using fault slip evolution from a kinematic waveform inversion as a boundary condition.
120 They applied the method to the 1995 Ms 6.8 Kobe (Japan) earthquake and examined
121 constitutive relations of fault slip, such as slip and/or slip-rate dependence of fault friction.
122 They found clear slip-weakening relations on the fault while no clear slip-rate dependence.
123 They analyzed the slip-weakening behavior and found a depth dependence of the critical
124 slip distance D_0 in the widely used slip-weakening law (Ida, 1972; Andrews, 1976; Day,
125 1982; Okubo and Dieterich, 1984; Ohnaka et al., 1987). Seismologically determined D_0
126 from this study is about 1 m or more in the shallow depth, while the upper limit is about
127 0.5 m or smaller in the deeper part of the fault. This method has also been used in later
128 studies, such as Piatanesi et al. (2004) and Ma (2021) for the 1999 Chi-Chi earthquake. In
129 this method, the absolute displacement of each wall of the fault interface, rather than the
130 slip (the relative displacement between the two walls), should be assigned as the boundary
131 conditions to calculate stresses. Ide and Takeo (1997) assume symmetry in displacement
132 between two walls and thus assign half of the slip to each wall. This assumption may be
133 largely valid for a vertical strike-slip fault. But it does not hold for dip-slip faults, in

particular shallow-dipping thrust faults, as the displacement of the hanging wall can be significantly larger than that of the footwall because of broken symmetry (Oglesby et al., 1998; Oglesby et al., 2000).

The third line of efforts is so called “fully dynamic inversions”. Peyrat and Olsen (2004) used dynamic rupture simulations and neighborhood algorithm (NA) to invert for stress drops for the 2000 Western Tottori earthquake (Mw6.6). In the dynamic inversion, stress drops are inverted on a number of rectangular patches over the fault plane, while assuming constant yield stress Tu and slip weakening distance D_0 over the fault plane. Di Carli et al. (2010) used low frequency strong motion data to do a nonlinear kinematic and dynamic inversion using NA for the 2000 Tottori earthquake. Both inversions are based on the elliptical subfault approximation to reduce model parameters. The kinematic inversion is used to establish a prior information to reduce parameters and define the parameter range for dynamic inversion. In the dynamic inversion, a strong prior constraint is applied by fixing the peak stress level Tu, initial stress field Te and slip weakening distance D_0. The inverted parameters are the geometries of two elliptical rupture patches. Ruiz and Madariaga (2011) proposed a dynamic inversion method for a moderate size of earthquake (Mw 6.7) in Chile. They assume a simple elliptical shape rupture patch and uniform stress and friction within the patch, and invert for eleven parameters in total, including five parameters for geometry, location, and orientation of the elliptical patch, two parameters for rupture initiation radius and (shear) stress level, four parameters for D_0, static strength Tu in the slip-weakening law, and initial (shear) stress levels inside and outside the patch. They perform forward dynamic rupture simulations by a finite different method and use a NA and Monte Carlo (MC) technique for the inversion. The method was used in later

studies for other intermediate sizes of earthquakes (Ruiz and Madariaga, 2013; Ruiz et al., 2017; Herrera et al., 2017). Overall, they need dynamic rupture simulations in their inversions with NA, and the number of dynamic rupture simulations are not fixed depending on the convergence speed in NA.

More recently, Xie and Cai (2018) proposed an earthquake stress model and applied it to invert for coseismic static stress changes on the shallow-dipping fault plane (including both fault shear and normal stresses) of the 2011 Mw 9.0 Tohoku (Japan) earthquake. They obtained the fault shear and normal stresses changes due to the earthquake directly from GPS data of the coseismic deformation, without the need of slip inversion as in Okada's method or Rapperger and Mai's method. In addition, they can obtain fault normal stress changes, which are absent in the Rapperger and Mai's method but can be significant in dip-slip faulting earthquakes such as the Tohoku earthquake. They further applied the method to invert for fault stress accumulations (both shear and normal stresses) directly from GPS data before the Tohoku earthquake, revealing large shear stress accumulations and normal stress variations in the Tohoku coseismic rupture areas (Xie et al., 2019).

In this study, we extend Xie and Cai's earthquake stress model to the dynamic process and present a fault-stress model of earthquake sources in the framework of the representation theorem, in comparison with the kinematic slip model of earthquake sources (i.e., the fault-slip model) that has been dominantly used in the community. We then develop a dynamic stress inversion method based on the fault-stress model to directly invert seismic waveform recordings for the coseismic fault stress evolution (both shear and normal stresses). Compared with the second line of efforts reviewed above, the method eliminates the need of the slip evolution inversion and avoids problematic assumptions

such as symmetric displacements between the two walls of a fault interface. Compared with the third line of efforts discussed above, the method does not need to perform spontaneously dynamic rupture modeling. Involvement of dynamic rupture modeling in these previous dynamic inversion methods makes them cumbersome and/or mainly applicable for intermedium sizes of earthquakes. In contrast, dynamic stress inversion methods based on the fault-stress model such as one proposed in this study can be standardized in a way similar to kinematic slip inversions that have been developed for many decades. The method can be used for small earthquakes to megathrust earthquakes. We test the method on a synthetic model and perform a resolution analysis with a checkerboard test. Finally, we apply it to the 2016 Mw 5.0 Cushing (Oklahoma) earthquake to show its validity. The fault-stress model and associated inversion methods such as one presented in this study open a door to decipher fault friction behavior and parameters such as D_0 directly from seismic recordings.

2. The fault-stress model of earthquake sources

2.1 The faulting theory of earthquakes and the fault-slip model

The faulting theory of earthquakes was established from observations of the extensive rupturing of the San Andreas fault during the 1906 San Francisco earthquake (Reid, 1910). In this theory, earthquakes are the results of dynamic faulting. This theory was proven to be valid for most shallow tectonic earthquakes by seismological and geodetic observations. The theory gained widespread acceptance since the early 1960s with the installation of the Worldwide Standardized Seismic Network (Scholz, 2002).

A faulting source of earthquakes has classically been characterized as slip across a fault plane, i.e., a discontinuity in tangential displacement. This is termed as the fault-slip model of earthquake sources in this study, in comparison with the fault-stress model to be developed. The fault-slip model has been the basis for kinematic slip inversions of seismic data in the literature. As shown in Figure 1, an internal interface (a fault plane) Σ with unit normal vector **n** (pointing from the Σ^- side to the Σ^+ side) is embedded in a volume V enclosed by surface S. The representation theorem gives the displacement **u(x,** t**)** at a general point **x** in the volume V at time t due to the sum of the contributions from slip history $[\boldsymbol{u}(\boldsymbol{\xi},\tau)]$ of points on the fault plane Σ in the Cartesian component form as (Aki and Richards, 1980, Eq. 3.2)

$$u_m(\boldsymbol{x},t) = \int_{-\infty}^{\infty} d\tau \iint_{\Sigma} [u_i(\boldsymbol{\xi},\tau)] c_{ijpq} n_j \partial G_{mp}(\boldsymbol{x}, t-\tau; \boldsymbol{\xi}, 0)/\partial \xi_q d\Sigma \qquad (1).$$

Here, $\boldsymbol{\xi}$ is the general position on the fault plane Σ, c_{ijpq} are elastic constants, n_j is the jth component of the unit normal vector **n** of Σ, G_{mp} is Green's function, and the Einstein's summation convention applies in the equation. Green's function $G_{mp}(\boldsymbol{x},t;\ \boldsymbol{\xi},\tau)$ gives the *m*th component of displacement at a general point **x** within V and time t due to unit slip in the *p*-direction at **x** = $\boldsymbol{\xi}$ on the fault Σ and t = τ.

Using the delta function derivative $\partial\delta(\boldsymbol{\eta}-\boldsymbol{\xi})/\partial\eta_q$ to localize points of Σ within V, Eq (1) may be written as

$$u_m(\boldsymbol{x},t) = \int_{-\infty}^{\infty} d\tau \iiint_{V} \left\{ -\iint_{\Sigma} [u_i(\boldsymbol{\xi},\tau)] c_{ijpq} n_j \partial\delta(\boldsymbol{\eta}-\boldsymbol{\xi})/\partial\eta_q d\Sigma \right\} G_{mp}(\boldsymbol{x}, t-\tau; \boldsymbol{\eta}, 0) dV \quad (2).$$

The term within {} in Eq (2) is the body-force equivalent of fault slip on Σ. Therefore, the seismic waves within V excited by fault slip are the same as those excited by a distribution

224 on the fault of certain body forces canceling moment, among which a surface distribution
225 of double couples can always be chosen in an isotropic medium (Aki and Richards, 1980,
226 Sec 3.2).
227
228 **2.2 The fault-stress model of earthquake sources**
229 Reid's (1910) seminal work led to the elastic rebound theory of tectonic earthquakes, in
230 which stress accumulation before an earthquake and stress drop (release) during an
231 earthquake are the key features of earthquake cycles. When shear stress increases to the
232 frictional strength level of a fault due to tectonic movement, the fault ruptures, releasing
233 the accumulated shear stress and generating fault slip and seismic waves. Therefore, in
234 principle a faulting source of earthquakes can also be characterized by shear stress drop,
235 more generally stress change, on the ruptured fault, in addition to slip across the fault plane.
236 But this concept had not been utilized until the recent study by Xie and Cai (2018), in
237 which they propose an earthquake stress model to study static stress changes of earthquakes.
238 Here, we extend their static earthquake stress model to the dynamic evolution of fault stress
239 during earthquakes. We term the model as the fault-stress model of earthquake sources, in
240 comparison with the fault-slip model reviewed above. Furthermore, we place this model in
241 the context of the representation theorem in seismology.
242 As shown in Figure 1, we consider the traction change $\Delta\boldsymbol{T}$ on the ruptured fault, instead
243 of fault slip, as the source of seismic waves. Here, we may consider two adjacent internal
244 surfaces, labeled Σ^- and Σ^+, which are opposite faces of the fault plane Σ. The traction
245 change $\Delta\boldsymbol{T}$ can be defined as the change in the traction $\boldsymbol{T}$, which is applied on Σ^- by the
246 material on the Σ^+ side. Then $-\Delta\boldsymbol{T}$, which is same in magnitude but opposite in direction

with $\Delta \boldsymbol{T}$, is the change in the traction $-\boldsymbol{T}$ that is applied on Σ^+ by the material on the Σ^- side. With this characterization of earthquake sources, we may write the representation of displacement at a general point **x** in volume *V* at time *t* due to the traction change on the ruptured fault as (i.e., the representation theorem for the new model)

$$u_m(\boldsymbol{x},t) = \int_{-\infty}^{\infty} d\tau \iint_{\Sigma} \Delta T_p(\boldsymbol{\xi},\tau) G_{mp}(\boldsymbol{x},t-\tau;\boldsymbol{\xi},0) d\Sigma \qquad (3).$$

Here, Green's function $G_{mp}(\boldsymbol{x},t;\boldsymbol{\xi},\tau)$ gives the *m*th component of displacement at a general point **x** within *V* and time *t* due to unit traction change in the *p*-direction at $\mathbf{x} = \boldsymbol{\xi}$ on the fault Σ and $t = \tau$. With this representation, we can invert for traction changes on the ruptured fault directly from seismic recordings, after Green's functions are calculated. As discussed above, this model is termed as the fault-stress model of earthquake sources in this study, which is the basis for a dynamic stress inversion method we develop below. Notice that $\Delta \boldsymbol{T}$ is a vector that generally does not lie within the fault plane Σ, i.e., non-zero values in both shear and normal components. Therefore, dynamic stress inversions based on this model can invert for both fault shear and normal stress changes of earthquakes from seismic recordings.

We remark that this new model, the fault-stress model of earthquake sources, is different from both double couples of earthquake sources and dynamic rupture models. Double couples are essentially a body-force equivalent of the fault-slip model, and fault slip is represented by a surface distribution of double couples. In the fault-stress model, the traction is surface force applied on the fault plane, not body force. Dynamic rupture models require friction laws, and rupture propagation is governed by these laws and stress and strength evolutions on the fault. Therefore, dynamic inversion procedures based on dynamic rupture models in the literature as reviewed above are cumbersome as they need

to handle rupture propagation and are limited in rupture geometry and earthquake sizes. In contrast, the fault-stress model developed here does not consider spontaneous rupture propagation. Instead, it only considers traction changes (i.e., fault shear and normal stress changes). Therefore, standard inversion procedures for dynamic stress evolutions can be developed relatively easily. For example, most techniques used in kinematic slip inversions over many decades can be readily adopted in dynamic stress inversion methods based on the fault-stress model, such as the one developed in the next section.

3. A dynamic stress inversion method

Based on the fault-stress model of earthquake sources, we develop a dynamic stress inversion method, which includes two major parts. The first part is to calculate the Green's functions at seismic stations due to unit stress changes over a finite time interval on individual fault patches (i.e., subfaults). We use an explicit finite element method (FEM) *EQdyna* (Duan and Oglesby, 2006; Duan and Day, 2008; Duan, 2010, 2012; Luo and Duan, 2018; Liu et al., 2018) to numerically calculate the Green's functions. The second part is to invert seismic waveforms directly for stress evolutions on all subfaults. We use a least-squares method with multiple physical constraints to perform the inversion.

3.1. Numerical Green's Function Calculations

To calculate numerical Green's functions at seismic stations, we divide the fault interface into many subfaults and apply unit stress changes (1MPa) on subfaults over a time interval along the fault strike, dip and normal directions, shown in Figure 2a. The model top boundary is set as free surface and other boundaries fixed. Perfectly matched layers (PML)

are used to absorb seismic wave reflection from truncated model boundaries (Liu and Duan, 2018). The initial-boundary value problem for such a numerical Green's function is governed by the following equations

$$\rho \Delta \ddot{u}_i = \Delta \sigma_{ij,j}, \quad (4)$$

$$\Delta \sigma_{ij} = \lambda \Delta \varepsilon_{kk} \delta_{ij} + 2\mu \Delta \varepsilon_{ij}, \quad (5)$$

$$\Delta \varepsilon_{ij} = (\Delta u_{i,j} + \Delta u_{j,i})/2, \quad (6)$$

$$\Delta \sigma_{ij} n_j | \Gamma_{subfault} = \Delta T_i, \quad (7)$$

$$\Delta \sigma_{ij} n_j | \Gamma_{free\_surface} = 0, \quad (8)$$

$$\Delta u_i n_i | \Gamma_{other_{boundary}} = 0, \quad (9)$$

$$\Delta u_i = 0 \, , (t = 0) \quad (10)$$

$$\Delta \dot{u}_i = 0 \, , (t = 0) \;\; (i, j = x, y, z). \quad (11)$$

where Δu_i , $\Delta \dot{u}_i$, $\Delta \ddot{u}_i$, $\Delta \sigma_{ij}$ and $\Delta \varepsilon_{ij}$ are changes in displacement, velocity, acceleration, stress and strain in the medium induced by a unit stress change applied to a subfault, respectively. λ and μ are Lame constants. n_i is the unit normal vector to the fault surface or a model boundary. ΔT_i is the applied unit stress change along i direction on a subfault. $\Gamma_{subfault}$ stands for the subfault interface and $\Gamma_{free\_surface}$ stands for the free surface of the model. δ_{ij} is the Kronecker delta and the Einstein's summation convection implies in the equations.

We solve the boundary value problem using *EQdyna*. The fault interface is modeled by the traction-at-split-nodes technique (Day et al., 2005; Duan, 2010). At each fault node location, the technique splits a fault node into two halves that share the same spatial location but can move relative to each other. The two halves of a split node interact only through a traction acting on the interface between them. Figure 2a schematically shows an

example that applies an along-strike unit stress change (ΔT_x) on a subfault of a strike-slip fault interface with two walls (Fault Wall A and B). The same concept applies to Green's functions for other subfault patches, arbitrary fault geometries, and unit stress changes along fault dip or fault normal directions. Notice that a subfault comprises two adjacent surfaces, on which stress changes are opposite in sign but same in magnitude. The unit stress change is applied over the first time-step in the dynamic simulation in Green's function calculations. The element size of a model is limited by the Courant-Friedrich-Lewy (CFL) condition (Courant et al., 1967) for the explicit time integration rule and by the need of frequency contents generated in the model. As a result, the dimension of a subfault is typically much larger than the element size to make model parameters in the inversion problem at a reasonable number relative to the number of available seismic recordings. Each subfault may contains tens of element facets, shown in Figure 2b. We apply a unit stress change uniformly on all the element facets within the subfault over the first time step. Then the resultant slip on all subfaults (three directions) and synthetic Green's functions on all available seismic stations (three directions) are stored for use in the inversion stage. This kind of computations is performed once before inversion for each subfault and for each stress change direction (strike, dip and normal), with the total number of calculations equal to the number of subfaults multiplied by three. The calculated Green's functions of seismic waves on available stations are used for dynamic stress inversion. The Green's functions of resultant slip on subfaults are used to apply constraints during the inversion and to recover the stress versus slip relation on each subfault after the inversion.

3.2 The Least-Squares Inversion with Constraints

We utilize the observed seismograms recorded by local stations to invert for the coseismic dynamic stress change history on each subfault and in each direction. For the inversion, the fault plane is divided into multiple subfaults (Figure 2b). On each subfault, the source time function (STF) is parameterized by several narrow stress change rectangles of the same duration and each rectangle offset by its duration, and the amplitudes of these stress change rectangles should be inverted (Figure 2c). On each subfault, we define a new local coordinate system to invert stress changes in three directions: $\mathbf{D_1}$, $\mathbf{D_2}$ and $\mathbf{D_n}$, shown in Figure 2b. The $\mathbf{D_1}$ and $\mathbf{D_2}$ are within the fault plane, with $\mathbf{D_1}$ as 45 degrees counterclockwise from the rake angle (rake-45) and $\mathbf{D_2}$ as 45 degrees clockwise from the rake angle (rake+45), while the $\mathbf{D_n}$ is perpendicular to the fault plane. In this way, the inverted stress changes of ΔT_1 and ΔT_2 (along $\mathbf{D_1}$ and $\mathbf{D_2}$ directions) are comparable in magnitude, which makes the inversion results more stable. The inverted ΔT_1 and ΔT_2 may be different, so that the rake angle of the resultant stress change vector (parallel with the fault plane) on each specific subfault may vary from the average rake angle (within 45 degrees).

To further stabilize inversion results, we also apply a smoothing constraint and a normal displacement continuity constraint in Eq (12), a non-negative slip constraint in Eq (13) and a moment constraint in Eq (14), as described below. The MATLAB routine lsqlin, which is a linear least-squares solver with bounds or linear constraints, is used to solve Equations (12)-(14).

$$\begin{bmatrix} \mathbf{G} \\ \lambda\mathbf{L} \\ \beta\mathbf{W} \end{bmatrix} \Delta\boldsymbol{T} = \begin{bmatrix} \boldsymbol{d} \\ \mathbf{0} \\ \mathbf{0} \end{bmatrix} \qquad (12)$$

$$\begin{bmatrix}\mathbf{S_1}\\ \mathbf{S_2}\end{bmatrix} \Delta\boldsymbol{T} >= \begin{bmatrix}\mathbf{0}\\ \mathbf{0}\end{bmatrix} \quad (13)$$

$$\begin{bmatrix}\mathbf{M_1}\\ \mathbf{M_2}\end{bmatrix} \Delta\boldsymbol{T} = \begin{bmatrix}\frac{\sqrt{2}}{2}\mathrm{m}_0\\ \frac{\sqrt{2}}{2}\mathrm{m}_0\end{bmatrix} \quad (14)$$

In above equations, $\Delta\boldsymbol{T}$ is the stress change vector to be inverted in the dynamic stress inversion, including stress changes on each subfault, each rectangle in source time function along each direction ($\mathbf{D_1}$, $\mathbf{D_2}$ and $\mathbf{D_n}$), as shown in Figure 2bc. In Eq (12), matrix **G** stores the Green's functions of three component seismic waves on available stations calculated by the FEM, which are generated by 1MPa stress change on each grid, each rectangle in source time function along each direction. Then the Green's functions in **G** matrix need to be convolved with a rectangle box function as designed in the STF. The vector ***d*** stores observed three component seismic waveforms at stations. Matrix $\lambda\mathbf{L}$ functions to apply a Laplacian regularization (Hartzell and Heaton, 1983; Yue and Lay, 2013), which constrains temporal and spatial smoothing of the inverted stress change STF. The optimal degree of smoothing is determined by iterative modeling of seismic waveforms using a range of smoothing factors λ. Matrix $\beta\mathbf{W}$ functions to apply the normal displacement continuity constraint with factor β. $\beta\mathbf{W}$ is equal to $\beta(\mathbf{S_n^A} - \mathbf{S_n^B})$ with $\mathbf{S_n^A}$ and $\mathbf{S_n^B}$ representing the normal displacement on all subfaults on Fault Wall A and Fault Wall B. In Eq (13), matrix $\mathbf{S_1}$ stores Green's functions of fault slip in the $\mathbf{D_1}$ direction on all subfaults, generated by 1 MPa stress change on each subfault, each rectangle in source time function and along each direction. Matrix $\mathbf{S_2}$ is similar to $\mathbf{S_1}$, representing the fault slip in the $\mathbf{D_2}$ direction. The non-negative slip constraint in Eq (13) regulates that final slip vector $\mathbf{S_1}\Delta\boldsymbol{T}$ along $\mathbf{D_1}$

and $\mathbf{S_2}\Delta\boldsymbol{T}$ along $\mathbf{D_2}$ should be equal or larger than zero, so that the direction of final fault slip on each subfault should be within 45 degrees from the earthquake rake angle, which is realistic and further stabilizes the dynamic stress inversion results. In Eq (14), matrices $\mathbf{M_1}$ and $\mathbf{M_2}$ store Green's functions of cumulative moment on the whole fault in the $\mathbf{D_1}$ and $\mathbf{D_2}$ directions, generated by 1MPa stress change on each subfault, each rectangle in source time function and along each direction. The vector on the right of Eq (14) is composed of two values, each equal to $(\sqrt{2}/2)m_0$, with scalar value m_0 equal to the moment of the target earthquake. The moment constraint in Eq (14) regulates that the total moment in the direction of rake angle is approximately equal to m_0, to avoid an anomalous inverted moment.

4. A synthetic model test

4.1 Forward modeling of the synthetic model A

We build a synthetic strike-slip model A based on the fault geometry and 1D seismic velocity structure of the 2016 Mw 5.0 Cushing earthquake (Meng et al., 2021) to test the dynamic stress inversion method. The fault of the 2016 Cushing earthquake is a vertical NEE strike-slip fault with its surface trace shown in Figure 3, and the 1D velocity structure is given in Table 1.

The synthetic strike-slip model A, shown in Figure 4, is generated using *EQdyna*. Model A has a strike-slip source patch in size of about 4.5 km by 4.5 km as shown in Figure 4ad, with the rupture starting at x = 4.0 km and z = -3.4 km and a fixed rupture velocity of ~3 km/s. The fault is governed by the time weakening friction law (Andrews, 2004) where the static friction coefficient f_s drops linearly to the dynamic friction coefficient f_d over 0.2

s. The time step is 0.01 s in the simulation. Within the source patch, static friction is $f_s = 0.4$ and dynamic friction is $f_d = 0.3$ in the center (2.5 km by 2.5 km) and linearly increases to $f_d = f_s = 0.4$ over 1km to the boundaries. Outside of the source patch $f_s = f_d = 0.4$. The initial normal and shear stress on the fault plane is set as -100 MPa (negative compressional) and 35 MPa, respectively, thus the source patch tends to yield stress drop (along strike) of about 6 MPa, and areas surrounding the stress drop zone have stress increase due to the termination of slip (Figure 4a). The stress increase zone is very narrow with the maximum stress increase about 7 MPa (Figure 4a). For a strike-slip model, the stress change amplitude is much smaller along the dip and normal directions, Figure 4bc. In addition to synthetic stress change model (Figure 4abc), the dynamic simulation generates synthetic slip distribution on fault interface (Figure 4def) and synthetic seismic waveforms at selected stations. The maximum synthetic slip along strike direction is about 0.4 m distributing within the source patch (Figure 4d), while the slip in the dip and normal directions are very small compared to the strike direction, Figure 4ef. From synthetic model A, we generate synthetic seismic waveforms on eight virtual stations evenly distributed on two sides of the fault trace (Figure 3a), and also on five virtual stations (Figure 3b), for the synthetic test.

4.2 Green's function generation

To calculate the numerical Green's functions for this synthetic model test, the following checkerboard test and the Cushing earthquake source inversion, we set a finite element model in size of 60 km by 60 km by 30 km along x, y, z directions, with element size of 100 m. We utilize an 1D velocity structure from the kinematic source inversion study of

the Cushing earthquake (Meng et al., 2021) and the P-wave velocity, S-wave velocity and density of different layers are presented in Table 1. Given the minimum S-wave velocity of 1.5 km/s in the top layer and assuming that we need at least 5 elements to resolve a wavelength, the highest frequency contents in the numerical Green's functions is 2.9 Hz. The total fault interface is 9 km by 6.5 km, in the x-z plane. We divide the fault interface into 18 by 13 subfaults along x and z directions, respectively, with each subfault in size of 500 m by 500 m. Given the element size of 100 m, each subfault comprises 5×5 quadrilateral element facets. Time step is calculated as $dt = \alpha dx/V_p$ according to the CFL condition (Courant et al., 1967). We choose $dt = 0.01\,s$ with $\alpha = 0.5$. The unit stress change of 1 MPa is applied at each subfault uniformly over the first time step, along fault normal, strike and dip directions, respectively. There are in total $18 \times 13 \times 3 = 702$ Green's functions computed on each of eight virtual stations (Figure 3a) for the synthetic model test and checkerboard test, and on each of five real stations (Figure 3b) for the synthetic model test, checkerboard test and the Cushing earthquake source inversion.

4.3 Inversion for the synthetic model A

Utilizing the synthetic seismic waveforms on eight virtual stations (Figure 3a), we apply the dynamic stress inversion method to invert model A as a benchmark test, using synthetic seismic waves generated in model A as virtual observations (***d*** vector in Eq. 12). In the inversion, we adopt the same hypocenter location at x = 4.0 km and z = -3.4 km and the same rupture velocity of 3 km/s as in the synthetic forward modeling in model A. The stress change source time function at each subfault is parameterized by four rectangles, each rectangle lasting for 0.2 s and offset by 0.2 s, with total duration of 0.8 s. We invert for the

amplitude of each rectangle to get the stress change history for each subfault along each direction. The total moment m_0 in model A is utilized for the moment constraint during the inversion (Eq. 14). Before inversion, both the Green's functions in matrix **G** and the virtual observed seismic waves in ***d*** are band-pass filtered between 0.5 - 2 Hz. During inversion, we use a range of smoothing factor λ to get the relationship between λ and the waveform matching misfit, as shown in Figure 5a, where the optimal λ is around $5*e^{-4}$. The β factor vs misfit is shown Figure 5b, while using $\lambda=5*e^{-4}$. Unlike the thrust fault situation in Xie and Cai (2018), the β factor has very small effect on the misfit for a strike-slip fault in this test, because the misfit only increases by 0.002 when β factor increases by several orders. Applying the λ factor of $5*e^{-4}$ and β factor of $1.5*e^{-6}$, the inverted result INV1 is shown Figure 6.

The inverted stress changes and associated fault slip along the strike, dip and normal directions (Figure 6) are close to those of the synthetic model A (Figure 4). The inverted result INV1 shows a maximum stress drop about -5.9 MPa and stress increase about 1.6MPa along strike direction (Figure 6a), compared with the maximum stress drop of -6MPa and stress increase about 7 MPa in the synthetic model (Figure 4a and Figure 7). The maximum inverted stress increase along strike is much lower than that in the synthetic model because the inverted stress change is an average value over a subfault with a size of 500 m, not to mention that a smoothing factor is also applied during the inversion, further averaging a sharp stress increase. For example, we compare the original stress change in model A with those after averaging over 500m and 1000 m along strike in Figure 7. After applying smoothing over 1000m, the maximum stress increase drops to about 2 MPa while the maximum stress drop stays unchanged in the center of the slip patch. The maximum

inverted fault slip along strike is around 0.33 m (Figure 6d), close to but smaller than that in the synthetic model A. In INV1, the inverted normal stress and slip are both near zero values, consistent with those in the synthetic model A due to a proper usage of constraint factor β. In addition, we use a pair of smaller parameters of $\lambda=1.5*e^{-4}$ and $\beta=1.5*e^{-7}$ to get the inverted result INV2 as a comparison with INV1, shown Figure 8. In INV2, the maximum inverted stress drop and increase are -7.3 MPa and 2.2 MPa. The maximum inverted slip along strike is around 0.38 m, closer to the maximum slip in synthetic model A than INV1. For two inverted results, the inverted slip patch size is slightly larger and maximum slip is slightly smaller compared to the synthetic model A, which may relate to the application of the smoothing factor. Generally, we need to utilize a smoothing factor closer to the optimal value, in order to avoid oversmoothing or undersmoothing by using a too large or too small λ, according to Xie and Cai (2018). The smoothing factors used in INV1 and INV2 are close to the optimal value, and the inverted results recover well the source features in the synthetic model. In INV2, the inverted normal stress and slip is larger due to a weaker normal slip continuity constraint when using a smaller β factor in INV2 than in INV1.

The two inversion cases INV1 and INV2 are both conducted under the condition of utilizing virtual seismic data on eight close stations, as shown in Figure 3a. We also conduct an inversion INV3 using virtual seismic data on five stations as shown in Figure 3b. The relative locations of five stations to the fault is set up based on the 2016 M 5 Cushing earthquake and its adjacent seismic stations, that we will present in later sections. In INV3 (Figure 9), we find that the inverted final stress change and resultant final fault slip is generally similar to those in INV1 and INV2. In addition, an artificial stress drop and slip

area occurs near the bottom of the fault zone, which is likely due to the lack of station coverage compared to INV1 and INV2. It implies an important role of the dense seismometer array for improving the resolution of dynamic stress inversions. Notice that the stress change inversion involves three traction components, while kinematic slip inversions only involve two slip components within the fault plane. Inversion for more parameters in the stress change inversion may require more high-quality observed data to get stable and reliable results.

4.3.1 Deciphering D_0

The dynamic stress inversion allows us to obtain the distribution of the critical slip distance D_0 in the slip-weakening law on the fault plane directly from seismic recordings. In Figure 10, we plot the stress versus slip curves from INV2 and compare them with those from the synthetic model A. We remark that in the synthetic model A, D_0 (turning point of the stress vs slip curve) varies on the fault plane with a smaller value (~0.05 m) near the hypocenter and larger values further away from the hypocenter (>0.1 m), because a time-weakening friction law (e.g., Andrews, 2004) is used in the synthetic forward modeling. The comparison shows that the dynamic stress inversion method can invert for D_0 values well, in particular near the hypocenter. It can also recover the spatial variation of D_0 on the fault plane. We notice that some subfaults further away from the hypocenter may have smaller inverted final stress drop values compared with the synthetic values, which may relate to the smoothing effect in the inversion. At the stress drop under-estimated points or some other stress drop over-estimated points, the turning point of D_0 gets blurred to some extent, compared with the synthetic model A.

5. Resolution analysis: A checkerboard test

To check the resolution of the dynamic stress inversion method, we conduct a checkerboard test with the same fault geometry and velocity structure as the above section. We first perform a dynamic rupture simulation using *EQdyna* to obtain the forward checkerboard source model and virtual waveforms at two sets of seismic stations (eight stations and five stations shown in Figure 3) . Then we utilize the Green's functions and apply the dynamic stress inversion method to obtain the inverted source model by matching the virtual waveforms.

The forward checkerboard model has a source composed of nine 2 km×2 km patches as shown in Figure 11ab. Similar to model A, the fault is governed by the time weakening friction law (Andrews, 2004) where the static friction coefficient f_s drops linearly to the dynamic friction coefficient f_d over 0.2 s, with time steps of 0.01 s. Five shaded patches out of nine have $f_s = 0.4$ and $f_d = 0.3$, while the other four have $f_s = f_d = 0.4$. Given a uniform initial normal and shear stress of -100 MPa (negative compressional) and 35 MPa, respectively, the five shaded patches yield stress drops of about 5 MPa, while outside of them stress increases sharply. The rupture is set to start at x = 4.0 km and z = -3.4 km with a fixed rupture velocity of 3 km/s. The shear stress change and associated slip distributions of the checkerboard model are shown in Figure 11ab. Uniform stress drops occur on the five shaded patches with sharp stress increases in the narrow zones immediately outside of the four outer patches. The associated slip distribution is heterogeneous with slip concentrated within the five shaded patches and larger slip at shallower depths.

Using the Green's functions calculated earlier (section 4.2) and the virtual seismic waveforms generated by the forward checkerboard model above, we invert for the stress

changes directly and calculate fault slip associated with the stress changes. The hypocenter and rupture velocity are set to be the same as the checkerboard forward model. The parameterization of the stress-change source time function and the bandpass filter applied to seismic waveforms are the same as those in the inversion of model A. When using eight stations, the patches and amplitudes of the stress drop are well recovered as shown in Figure 11c. The patches of slip are well recovered (Figure 11d), though inverted slip amplitudes are smaller than the synthetic values (Figure 11b) . With five stations, the stress drop and slip patches are less well recovered (Figure 11ef) because of fewer stations and poor station coverage. Generally, the shallower three patches are recovered while the two deeper patches suffer a low resolution.

6. Application to the 2016 Mw 5.0 Cushing (Oklahoma) earthquake

We apply the dynamic stress inversion method to the 2016 M 5 Cushing earthquake. The M5 Cushing earthquake occurred on November 7th, 2016, near the city of Cushing in Oklahoma, which is the largest crude oil storage site in the USA, and also close to numerous water disposal wells. There are many nearby stations for this event, but only 5 stations are within epicentral distance of 10 miles. We use seismic recordings at these 5 stations to perform the dynamic stress inversion with Green's functions calculated in Section 4.2. The fault geometry (strike/dip/rake 60°/90°/0°), hypocenter location (3.4 km depth) and rupture speed (3km/s) are consistent with the previous kinematic study of this event (Meng et al., 2021). Total fault dimension is of 6.5×6.5 km, with each subfault size of 0.5×0.5 km. On each subfault, the STF is composed by four 0.2 s rectangles. The inverted final shear stress change and associated fault slip from the dynamic inversion are

shown in Figure 12ab. There are two separate stress drop (and slip) patches on the fault plane: one near the hypocenter and the other to the north (right) of the first patch, reflecting a complex rupture pattern even for a M 5 event. From the stress vs slip curves near the centers of two slip patches, we find the stress drop and slip weakening distance D_0 are larger near the hypocenter (Figure 12c) than in the second slip patch (Figure 12d).

For the 2016 Cushing earthquake, Meng et al. (2021) inverted a kinematic slip model. They further calculated the static stress change using the Coulomb3 software (Toda et al., 2011) based on the inverted slip on each subfault. Comparing results from two methods, they both obtain two main slip/stress-drop patches with similar relative locations. The inverted slip patches from the dynamic stress change inversion are slightly larger than those from the kinematic slip inversion, and the maximum value of the stress drop and slip is lower in the dynamic stress change inversion result. This difference may be related to more model parameters in the dynamic stress inversion, for the given available data. In addition, we do not capture frequency contents higher than 3 Hz in the numerical Green's function calculations in order to reduce computational costs, and the bandpass filtering applied for both observation and Green's function waveforms is 0.2-2 Hz for the dynamic stress inversion. For the kinematic slip inversion, the Green's functions, calculated based on a semi-analytical method (Zhu and Rivera, 2022), can carry very high frequency signal and both observation and Green's function waveforms are bandpass filtered to higher frequency band (0.2-3Hz) for the Cushing earthquake (Meng et al., 2021).

7. Discussion

Compared with other fully dynamic inversions (the third line of efforts in Introduction), which need to run dynamic rupture simulations many times during the inversion process,

we only need to calculate numerical Green's functions, the most time-consuming part, once through the whole inversion process. Because the forward numerical modeling is separated from the inversion part, similar to the kinematic inversion, we don't need to make priori assumptions, for example the yield strength, stress drop or friction parameters, to reduce inversion parameters or narrow down the parameter space. In addition, we invert not only for shear stress change but also for normal stress change, which could be significant in megathrust events (Xie and Cai, 2018).

Compared with the static and dynamic stress inversion methods based on kinematic inversion results (the first and second lines of efforts in Introduction), we utilize physics-based models to calculate stress change Green's functions and directly fit the seismic data instead of fitting preexisting kinematic slip models. If utilizing fault slip as input, the uncertainties in slip from kinematic inversions will map into stress results. Furthermore, some methods (e.g. Ide and Takeo, 1997) must split fault slip onto the two sides of the fault to solve for the stress change, which may be very difficult (or not valid) for dip-slip faulting earthquakes such as megathrust events, in which the hanging wall has much larger displacement than the footwall. In addition, our finite element models for Green's function calculations can capture complex geometry of earthquake faults and use heterogeneous velocity structures, unlike some analytical methods that require a homogeneous medium and/or simple fault geometry.

We remark that we need to find a balance between the computation efficiency and inversion resolution in the dynamic stress inversion. In the dynamic inversion, the source time function needs to convolve with the stress change Green's function to fit the recorded seismograms. For Green's function calculations with the FEM, finer element sizes are

needed for higher frequency contents, which could be computationally demanding. In addition, we parameterize the source time function by several consecutive nonoverlapping rectangles in this study. This represents a piecewise linear stress evolution over each rectangle duration (for example 0.2 s in this study). It would be interesting to test other types of source time function in future studies, such as trapezoid for nonlinear stress evolution. Finally, during Green's function calculations a unit stress change of 1 MPa is applied at each subfault uniformly over the first time step, under assumption that a small subfault can be regarded as moving simultaneously. In the future, if we study large megathrust earthquakes with much larger subfault dimension, e.g. 10 by 10 km in size, we need to consider the rupture prorogation effect when calculating Green's functions on each subfault.

One important contribution of the fault-stress model and the dynamic stress inversion method developed in this study is to open a door for the scientific community to study fault friction behaviors directly from seismic recordings, in addition to dominantly laboratory studies of fault friction in the literature. As shown in the synthetic and the real case (Cushing) tests above, we can recover the slip-weakening process and the associate parameter value (the critical slip distance D_0) well. With more studies in the future, we may be able to examine rate- and state-dependence of fault friction directly from seismic observations, paving a way for finding parameter values of fault friction that are directly applicable to natural earthquakes, instead of extrapolating laboratory experiment results on small rock samples to natural earthquakes, which is a challenging and classical scaling problem in geoscience.

The dynamic stress inversion method developed in this study shares common techniques with classical kinematic slip inversion methods. In principle, techniques for kinematic slip inversions that have been developed over many decades in the community can be readily used for a dynamic stress inversion based on the fault-stress model presented in Section 2. The dynamic inversion method we develop in this study and its tests on the synthetic, checkerboard models and the Cushing earthquake show that the fault-stress model works well. We encourage many colleagues in seismology to apply their kinematic slip inversion methods and techniques they develop over years to perform dynamic stress inversions of recent earthquakes, based on the fault-stress model presented in this study, to decipher more physics from past earthquakes. It is our hope that this study provides a new paradigm for the scientific community to perform seismic source inversions and study earthquake source physics.

8. Conclusions

In this study, we present a fault-stress model of earthquake sources, in comparison with the fault-slip model that dominates in earthquake source studies. Based on the fault-stress model, we develop a dynamic stress inversion method to invert for the coseismic stress evolution on the fault directly from seismic recordings. In this method, numerical Green's functions at seismic stations are calculated by an explicit finite element method *EQdyna* for a unit change of shear or normal stress on each sub-fault patch. Although computationally demanding, they can be computed efficiently with high-performance supercomputers and require only one time calculation. We apply several constraints, including zero normal slip (no separation or penetration of the fault), non-negative shear

slip (positive or zero shear slip), and moment constraints to invert for the dynamic stress evolution with a least-squares method. Tests on a synthetic model, a checkerboard model and the real dataset from the 2016 M 5 Cushing (Oklahoma) earthquake, show that the method recovers well the dynamic stress changes during an earthquake with reliable performance. We expect that the fault-stress model and associated dynamic stress inversion methods such as one developed in this study will improve seismic source inversions significantly from a dynamic point of view. They provide the scientific community with a new paradigm to study fault frictional behaviors, which govern dynamic rupture propagation, directly from seismic recordings. In addition to recovering the critical slip distance D_0 in the slip-weakening friction law as shown in this study, we may be able to decipher rate- and state- dependence of fault friction and corresponding parameter values that are applicable to natural earthquakes directly from seismic data in the future.

Acknowledgements

This research is supported by NSF grants EAR-2013695 and EAR-2147340. The authors appreciate Texas A&M High Performance Research Computing (https://hprc.tamu.edu) for providing the advanced computer resources used in this study.

Data Availability Statement

The data supporting the analysis and conclusions is given in figures and tables, in the main text and Supporting Information. The *EQdyna* code used in this study is available at https://github.com/dunyuliu/EQdyna. The waveform data for 2016 Cushing earthquake are

681 downloaded from Incorporated Research Institutions of Seismology (IRIS,
682 https://www.iris.edu/hq/).
683
684
685 **References**

686 Ammon, C. J., et al. (2005), Rupture process of the 2004 Sumatra-Andaman
687 earthquake, *Science*, 308, 1133–1139, doi:10.1126/science.1112260.
688 Andrews, D. J. (1976), Rupture velocity of plane strain shear cracks, J. Geophys. Res., 81,
689 5679–5687.
690 Andrews, D.J. (1980), Fault impedance and earthquake energy in the Fourier transform
691 domain. Bulletin of the Seismological Society of America 70, 1683–1698..
692 doi:10.1785/bssa0700051683
693 Andrews, D.J. (2004), Rupture models with dynamically determined breakdown
694 displacement. Bull. Seismol. Soc. Am. 94, 769-775.
695 Aki, K., P. Richards, *Quantitative Seismology*, 932, W. H. Freeman, New York, 1980.
696 Beroza, G. C., and P. Spudich (1998), Linearized inversion for fault rupture behavior:
697 Application to the 1984 Morgan Hill, California, earthquake, J. Geophys. Res., 83,
698 6275-6296.
699 Bouchon, M. (1997), The state of stress on some faults of the San Andreas system as
700 inferred from near-field strong motion data, J. Geophys. Res., 102, 11731-11744.
701 Bouchon, M., M. Campillo, and F. Cotton (1998), Stress field associated with the rupture
702 of the 1992 Landers, California, earthquake and its implication concerning the fault

703 strength at the onset of the earthquake, J. Geophys. Res., 103, 21,091–21,097,
704 doi:10.1029/98JB01982.
705 Day, S. M. (1982), Three-dimensional simulation of spontaneous rupture: The effect of
706 nonuniform prestress, Bull. Seismol. Soc. Am., 72, 1881–1902.
707 Day, S.M., Dalguer, L.A., Lapusta, N., Liu, Y. (2005), Comparison of finite difference and
708 boundary integral solutions to three-dimensional spontaneous rupture. Journal of
709 Geophysical Research-Solid Earth 110.
710 Di Carli, S., François-Holden, C., Peyrat, S., Madariaga, R. (2010), Dynamic inversion of
711 the 2000 Tottori earthquake based on elliptical subfault approximations. Journal of
712 Geophysical Research: Planets 115. doi:10.1029/2009jb006358.
713 Duan, B., and D. D. Oglesby (2006), Heterogeneous fa 734 ult stresses from previous
714 earthquakes and the effect on dynamics of parallel strike-slip faults, J. Geophys. Res.,
715 111(B5), doi:10.1029/2005JB004138.
716 Duan, B., and S. M. Day (2008), Inelastic strain distribution and seismic radiation from
717 rupture of a fault kink, J. Geophys. Res., 113(B12), doi:10.1029/2008JB005847.
718 Duan, B., 2010. Role of initial stress rotations in rupture dynamics and ground motion: A
719 case study with implications for the Wenchuan earthquake. J. Geophys. Res. 115.
720 Duan, B. (2012), Dynamic rupture of the 2011 Mw 9.0 Tohoku-Oki earthquake: Roles of
721 a possible subducting seamount, J. Geophys. Res., 117(B5),
722 doi:10.1029/2011JB009124.
723 Harris, R.A., Barall, M., Aagaard, B., Ma, S., Roten, D., Olsen, K., Duan, B., Liu, D., Luo,
724 B., Bai, K., Ampuero, J.P., Kaneko, Y., Gabriel, A.A., Duru, K., Ulrich, T., Wollherr,
725 S., Shi, Z., Dunham, E., Bydlon, S., Zhang, Z., Chen, X., Somala, S.N., Pelties, C.,

726 Tago, J., Cruz-Atienza, V.M., Kozdon, J., Daub, E., Aslam, K., Kase, Y., Withers, K.,
727 Dalguer, L., 2018. A Suite of Exercises for Verifying Dynamic Earthquake Rupture
728 Codes. Seismol. Res. Lett. 89, 1146-1162.
729 Herrera, C., Ruiz, S., Madariaga, R., Poli, P., 2017. Dynamic inversion of the 2015 Jujuy
730 earthquake and similarity with other intraslab events. Geophysical Journal International
731 209, 866–875.. doi:10.1093/gji/ggx056
732 Fukuyama, E., and T. Mikumo, Dynamic rupture analysis: Inversion for the source process
733 of the 1990 Izu-Oshima, Japan, earthquake (M =6.5), J. Geophys. Res., 98, 6529-6542,
734 1993.
735 Hartzell, S. H., and T. H. Heaton (1983), Inversion of strong ground motion and teleseismic
736 waveform data for the fault rupture history of the 1979 Imperial Valley, California,
737 earthquake, Bull. Seismol. Soc. Am., 73, 1553-1583.
738 Hartzell, S.H., Heaton, T.H., 1986. Rupture history of the 1984 Morgan Hill, California,
739 earthquake from the inversion of strong motion records. Bulletin of the Seismological
740 Society of America 76, 649–674.. doi:10.1785/bssa076003064
741 Ide, S., Takeo, M., 1997. Determination of constitutive relations of fault slip based on
742 seismic wave analysis. Journal of Geophysical Research: Planets 102, 27379–27391..
743 doi:10.1029/97jb02675
744 Ji, C., Helmberger, D.V., Wald, D.J., Ma, K.-F., 2003. Slip history and dynamic
745 implications of the 1999 Chi-Chi, Taiwan, earthquake. Journal of Geophysical
746 Research: Atmospheres 108, n/a–n/a.. doi:10.1029/2002jb001764
747 King, G.C.P., R.S. Stein, and J. Lin, Static stress changes and the triggering of earthquakes,
748 Bull. Seismol. Soc. Amer., 84 (3), 935-953, 1994.

749 Lin, J., and R.S. Stein, Stress triggering in thrust and subduction earthquakes, and stress
750 interaction between the southern San Andreas and nearby thrust and strike-slip faults,
751 J. Geophys. Res., 109, B02303, doi:10.1029/2003JB002607, 2004.
752 Liu, D.Y., Duan, B.C., 2018. Scenario Earthquake and Ground-Motion Simulations in
753 North China: Effects of Heterogeneous Fault Stress and 3D Basin Structure. Bull.
754 Seismol. Soc. Am. 108, 2148-2169.
755 Luo, B., and B. Duan (2018), Dynamics of Non-planar Thrust Faults Governed by Various
756 Friction Laws, J. Geophys. Res. Solid Earth, doi:10.1029/2017JB015320.
757 Luttrell, K. M., X. Tong, D. T. Sandwell, B. A. Brooks, and M. G. Bevis (2011), Estimates
758 of stress drop and crustal tectonic stress from the 27 February 2010 Maule, Chile,
759 earthquake: Implications for fault strength, J. Geophys. Res., 116, B11401,
760 doi:10.1029/2011JB008509.
761 Ma, K.-F., Song, T.-R.A., Lee, S.-J., Wu, H.-I., 2000. Spatial slip distribution of the
762 September 20, 1999, Chi-Chi, Taiwan, Earthquake (MW7.6) -Inverted from
763 teleseismic data. Geophysical Research Letters 27, 3417–3420..
764 doi:10.1029/2000gl011393
765 Ma KF. (2021) A Review of the 1999 Chi-Chi, Taiwan, Earthquake from Modeling,
766 Drilling, and Monitoring with the Taiwan Chelungpu-Fault Drilling Project. In: Lo CH.,
767 Xu X., Chang WY., Ando M. (eds) Earthquake Geology and Tectonophysics around
768 Eastern Tibet and Taiwan. Atmosphere, Earth, Ocean & Space. Springer, Singapore.
769 https://doi.org/10.1007/978-981-15-6210-5_4.

770 Meng, Q., Ni, S., Peng, Z., 2021. Complex Source Behaviors and Spatiotemporal Evolution
771 of Seismicity During the 2015–2016 Earthquake Sequence in Cushing, Oklahoma.
772 Journal of Geophysical Research: Solid Earth 126.. doi:10.1029/2021jb022168
773 Miyatake, T., 1992. Reconstruction of dynamic rupture process of an earthquake with
774 constraints of kinematic parameters. Geophysical Research Letters 19, 349–352..
775 doi:10.1029/92gl00082.
776 Oglesby, D. D., R. J. Archuleta, and S. B. Nielsen (1998), Earthquakes on dipping faults:
777 the effects of broken symmetry, *Science*, *280*, 1055-1059.
778 Oglesby, D. D., R. J. Archuleta, and S. B. Nielsen (2000), The three-dimensional dynamics
779 of dipping faults, *Bulletin of the Seismological Society of America*, *90*, 616-628.
780 Ohnaka, M ., Y. Kuwahara, and K. Yamamoto, Constitutive relations between dynamic
781 physical parameters near a tip of the propagating slip zone during stick-slip shear
782 failure, Tectonophysics, 144, 109-125, 1987.
783 Okada, Y., Internal deformation due to shear and tensile faults in a half-space, Bull.
784 Seismol. Soc. Amer., 82 (2), 1018-1040, 1992.
785 Okubo, P . G., and J. H. Dieterich, Effects of physical fault properties on frictional
786 instabilities produced on simulated faults, J . Geophys. Res., 89, 5817-5827, 1984.
787 Olson, A.H., Apsel, R.J., 1982. Finite faults and inverse theory with applications to the
788 1979 Imperial Valley earthquake. Bulletin of the Seismological Society of America 72,
789 1969–2001.. doi:10.1785/bssa07206a1969
790 Peyrat, S., Olsen, K.B., 2004. Nonlinear dynamic rupture inversion of the 2000 Western
791 Tottori, Japan, earthquake. Geophysical Research Letters 31, n/a–n/a..
792 doi:10.1029/2003gl019058

Piatanesi, A., 2004. The dependence of traction evolution on the earthquake source time function adopted in kinematic rupture models. Geophysical Research Letters 31. doi:10.1029/2003gl019225

Quin, H., Dynamic stress drop and rupture dynamics of the October 1979 Imperial Valley, California, earthquake, Tectonophysics, 175, 93-117, 1990.

Reid, H. F. (1910). The mechanism of the earthquake. In *The California earthquake of April 18, 1906, Report of the State Earthquake Investigation Commission*, Vol. 2. Washington, DC: Carnegie Institution, pp. 1-192.

Ripperger, J., Mai P. M., 2004. Fast computation of static stress changes on 2D faults from final slip distributions. Geophysical Research Letters 31. doi:10.1029/2004gl020594

Ruiz, S., Madariaga, R., 2011. Determination of the friction law parameters of the Mw 6.7 Michilla earthquake in northern Chile by dynamic inversion. Geophysical Research Letters 38, n/a–n/a.. doi:10.1029/2011gl047147.

Ruiz, S., Madariaga, R., 2013. Kinematic and Dynamic Inversion of the 2008 Northern Iwate Earthquake. Bulletin of the Seismological Society of America 103, 694–708. doi:10.1785/0120120056.

Ruiz, S., Aden-Antoniow, F., Baez, J.C., Otarola, C., Potin, B., Del Campo, F., Poli, P., Flores, C., Satriano, C., Leyton, F., Madariaga, R., Bernard, P., 2017. Nucleation Phase and Dynamic Inversion of the Mw 6.9 Valparaíso 2017 Earthquake in Central Chile. Geophysical Research Letters 44, 10, 290–10, 297. doi:10.1002/2017gl075675

Toda, S., R. S. Stein, V. Sevilgen, and J. Lin, 2011. Coulomb 3.3 Graphic-Rich Deformation and Stress-Change Software for Earthquake, Tectonic, and Volcano Research and Teaching – User Guide, *U. S. Geol. Surv. Open-File Rep. 2011-1060*.

816 Wald, D.J., and T.H. Heaton, Spatial and temporal distribution of slip for the 1992 Landers,
817 California, earthquake, Bull. Seismol. Soc. Am., 84, 668-691, 1994.
818 Wang, T., Wei, S., Shi, X., Qiu, Q., Li, L., Peng, D., Weldon, R. J., & Barbot,
819 S. (2018). The 2016 Kaikoura earthquake: Simultaneous rupture of the subduction
820 interface and overlying faults. *Earth and Planetary Science Letters*, **482**, 44–
821 51. https://doi.org/10.1016/j.epsl.2017.10.056
822 Wang, X., Wang, J., Zhang, C., 2022. A Broadband Kinematic Source Inversion Method
823 Considering Realistic Earth Models and Its Application to the 1992 Landers
824 Earthquake. Journal of Geophysical Research: Solid Earth 127..
825 doi:10.1029/2021jb023216
826 Xie, Z., Cai, Y., 2018. Inverse Method for Static Stress Drop and Application to the 2011
827 Mw9.0 Tohoku-Oki Earthquake. Journal of Geophysical Research: Solid Earth 123,
828 2871–2884.. doi:10.1002/2017jb014871
829 Xie, Z., Cai, Y., Wang, C.-y., Yoshioka, S., Tanaka, M., 2019. Fault stress inversion reveals
830 seismogenic asperity of the 2011 Mw 9.0 Tohoku-Oki earthquake. Scientific Reports
831 9, 11987.
832 Yamazaki, Y., Lay, T., Cheung, K.F., Yue, H., Kanamori, H., 2011. Modeling near-field
833 tsunami observations to improve finite-fault slip models for the 11 March 2011 Tohoku
834 earthquake. Geophysical Research Letters 38, n/a–n/a.. doi:10.1029/2011gl049130
835 Yue, H., Lay, T., 2011. Inversion of high-rate (1 sps) GPS data for rupture process of the
836 11 March 2011 Tohoku earthquake (Mw9.1). Geophysical Research Letters 38, n/a–
837 n/a.. doi:10.1029/2011gl048700

838 Yue, H., and T. Lay, 2013. Source rupture models for the Mw 9.0 2011 Tohoku earthquake
839 from joint inversions of high-rate geodetic and seismic data, Bull. Seismol. Soc. Am.,
840 103, 1242–1255, doi:10.1785/0120120119.
841 Yoshimoto, M., Yamanaka, Y., 2014. Teleseismic inversion of the 2004 Sumatra-
842 Andaman earthquake rupture process using complete Green's functions. Earth, Planets
843 and Space 66.. doi:10.1186/s40623-014-0152-4
844 Zhu, L., and L. Rivera, 2002. A note on the dynamic and static displacements from a point
845 source in multilayered media, *Geophys. J. Int.*, **148(3)**, 619– 627.
846
847

Tables and Figures

Table 1. 1D Velocity Structure used in this study, based on the case for the 2016 M 5 Cushing earthquake.

Depth (km)	Thickness (km)	Vp (km/s)	Vs (km/s)	Density (g/cm^3)
0.20	0.20	3.10	1.50	2.30
0.40	0.20	3.30	1.68	2.35
0.60	0.20	3.50	1.86	2.38
0.80	0.20	3.70	2.04	2.41
1.00	0.20	4.00	2.31	2.46
1.20	0.20	4.34	2.53	2.51
1.40	0.20	4.69	2.75	2.56
1.60	0.20	5.03	2.96	2.61
1.80	0.20	5.38	3.18	2.65
4.73	2.93	5.72	3.40	2.60
10.73	6.00	6.18	3.62	2.80
14.73	4.00	6.32	3.67	2.80
24.73	20.00	6.60	3.70	2.90
35.73	11.00	7.30	4.00	3.10
——	——	8.20	4.70	3.40

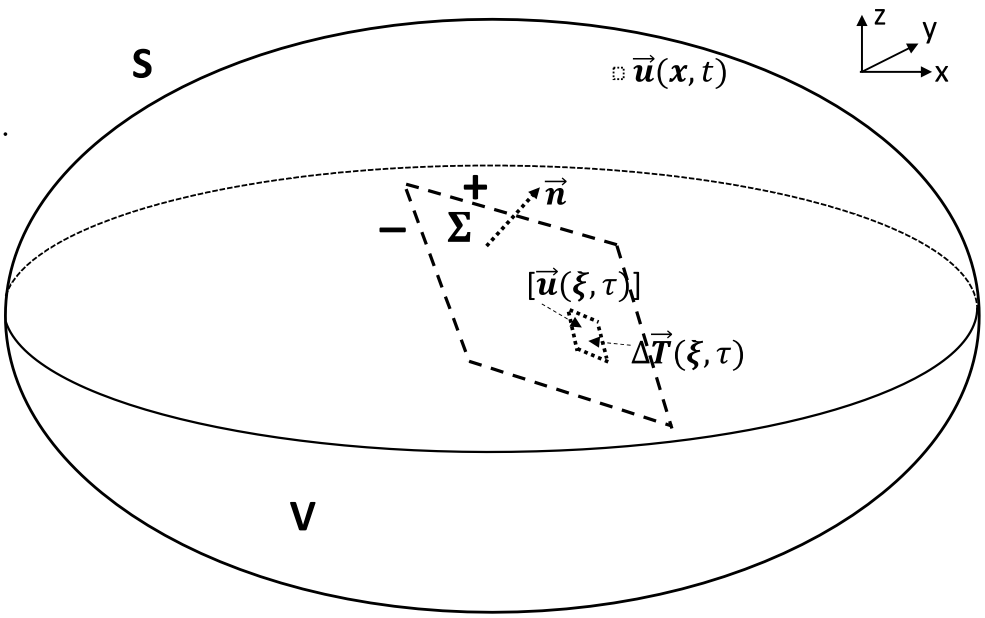

Figure 1. Schematic diagram for the fault-slip model and the fault-stress model of earthquake sources. A fault plane Σ, an internal surface with a unit normal vector **n** pointing from the – side (Σ^-) to the + side (Σ^+), is embedded within volume V that is enclosed by surface S. Dynamic faulting on Σ causes an earthquake, setting up seismic waves that propagate within V and can be recorded at a general point **x** within *V* (e.g., displacement **u**(**x**,t)). The fault-slip model of dynamic faulting characterizes the earthquake source as slip [**u**], i.e., the differential displacement between the two sides of the fault. The fault-stress model characterizes the earthquake source as traction change $\Delta\boldsymbol{T}$. Slip and traction change at a general point ξ on Σ are illustrated in the diagram.

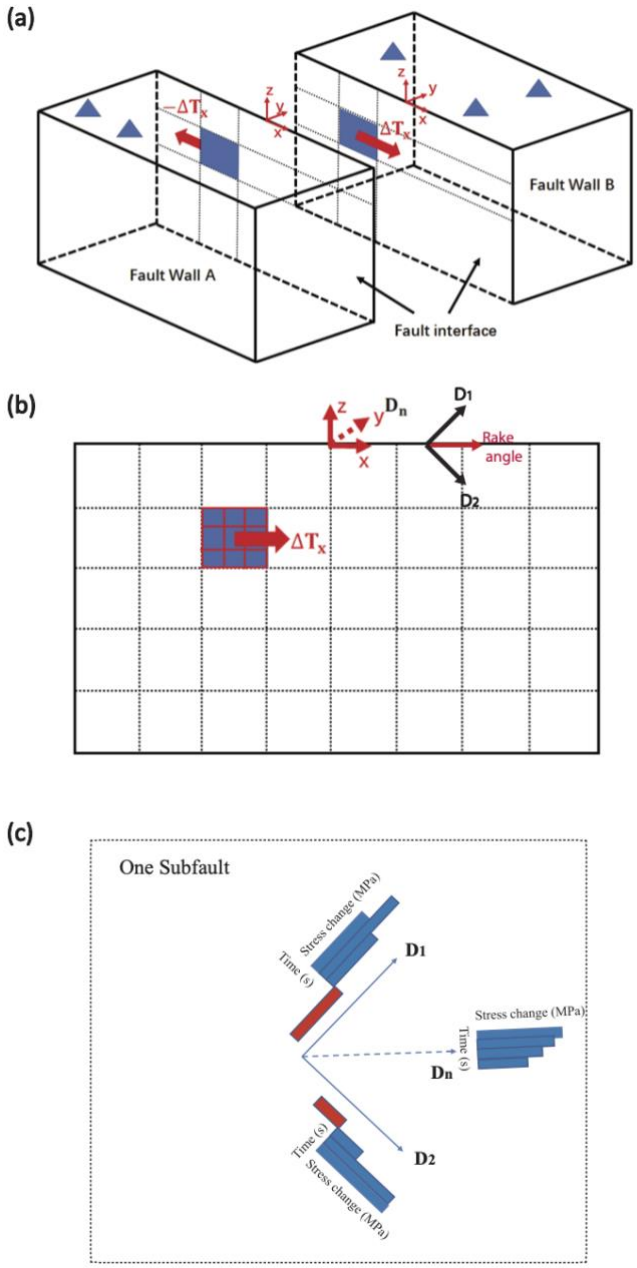

869

870 Figure 2. (a) A schematic diagram of the model for numerical Green's functions, which are
871 calculated by applying unit stress changes on subfaults. The two fault walls, which are
872 separated for a better visualization, are connected by tractions on the fault interface. The
873 shaded patches show the two surfaces of a subfault with a unit of stress change ΔT_x along
874 the x direction applied. The unit stress change of ΔT_x on fault wall B is in the opposite
875 sign to that on the fault wall A. Triangles on the free surface indicate stations recording

seismograms. The coordinate system of the finite element model is shown. (b) A detailed sketch of the fault interface on fault wall B. In the schematic case, the fault is divided into 5 by 8 subfaults. A unit stress change along the x direction ΔT_x is applied to the shaded subfault. The shaded subfault consists of 9 elements. The coordinate system of the finite element model is shown by **x**, **y**, **z**. A local coordinate system is defined by $\mathbf{D_1}$, $\mathbf{D_2}$ and $\mathbf{D_n}$, where $\mathbf{D_1}$ is 45 degrees counterclockwise with the earthquake rake angle (rake-45), $\mathbf{D_2}$ is 45 degrees clockwise to the earthquake rake angle (rake+45) and $\mathbf{D_n}$ is normal to the fault plane, parallel with **y** direction in this diagram. (c) A schematic diagram of the stress change source time functions, to be inverted, each composed of four rectangles, along three directions ($\mathbf{D_1}$, $\mathbf{D_2}$ and $\mathbf{D_n}$) on one subfualt interface on fault wall B. In this schematic case, blue rectangles represent stress drops and red rectangles represent stress increases. Direction $\mathbf{D_n}$ is perpendicular to the fault plane (into the paper).

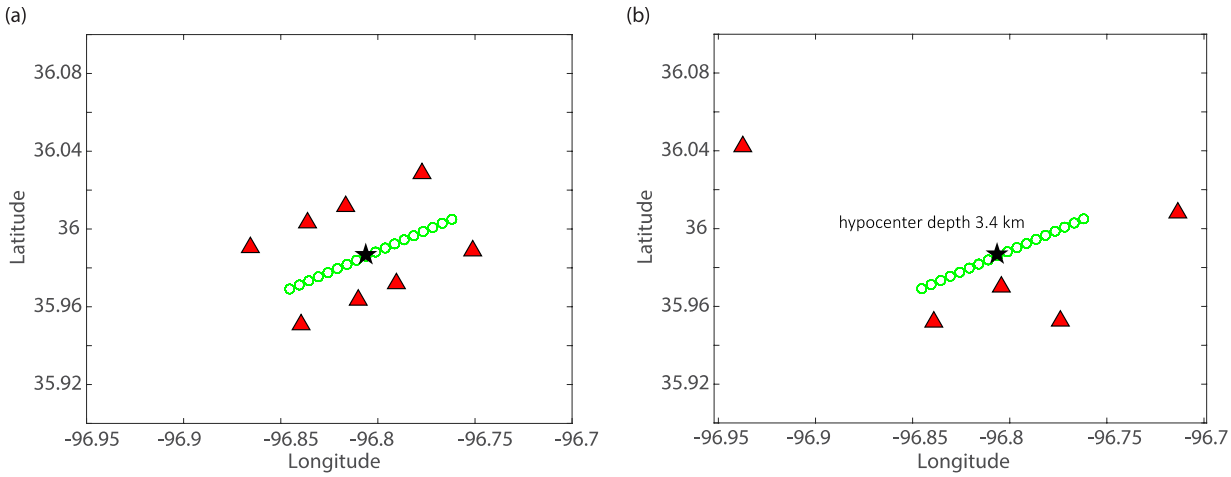

Figure 3. Surface trace of the vertical strike-slip fault (green circle chains) responsible for the 2016 M 5 Cushing (Oklahoma) earthquake with (a) eight virtual seismic stations distributed on two sides of the fault trace, and (b) five actual seismic stations that records the 2016 Cushing earthquake.

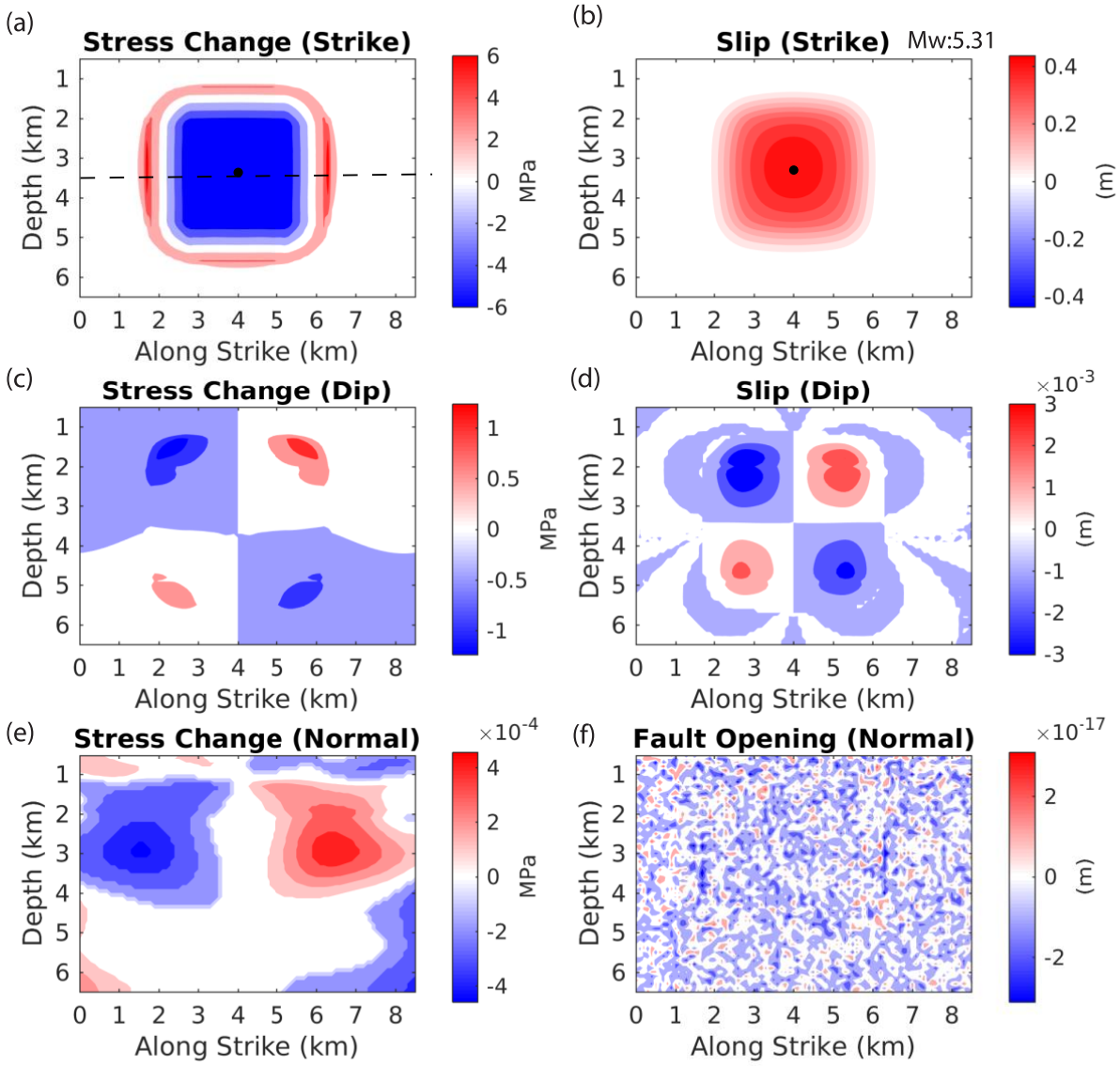

Figure 4. Final stress changes along (a) strike, (c) dip and (e) normal directions of the synthetic rupture model A generate by FEM and associated fault slip in (b) strike, (d) dip and (f) normal directions. The maximum slip is ~0.4 m and event magnitude is ~Mw 5.31. The black dots shown in (a) and (d) represent the rupture initiation point in model A. The shear stress profile shown by the dashed line in (a) is displayed in Fig. 7.

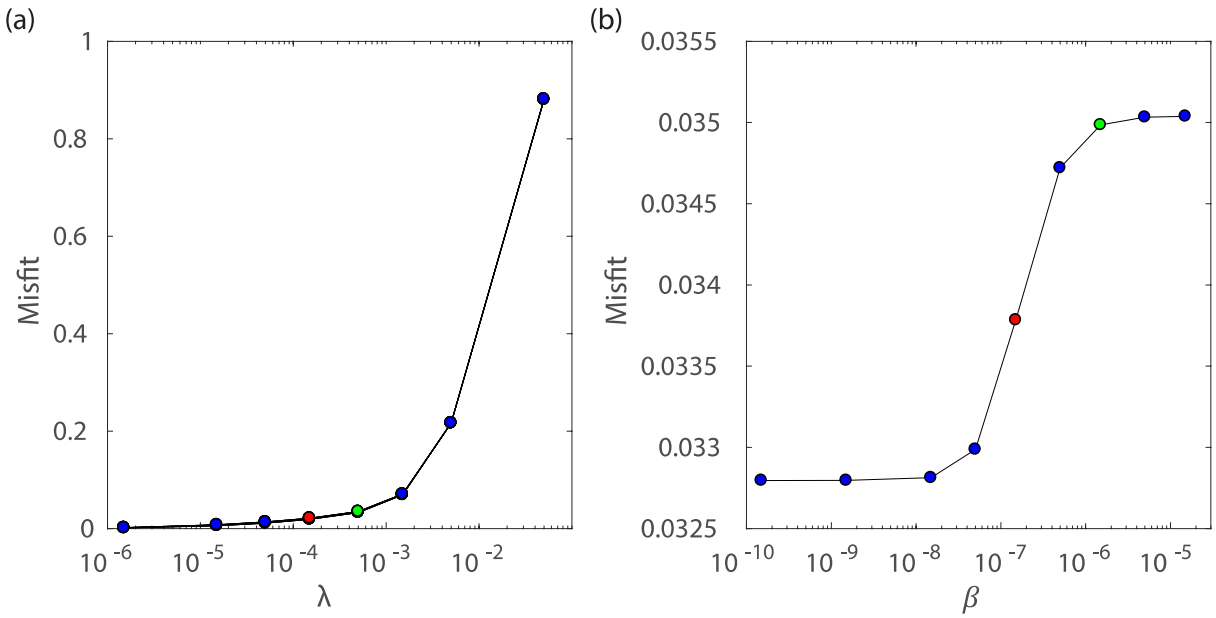

Figure 5. (a) Relationship of smoothing factor λ vs misfit (for waveforms on eight virtual stations), while using nine different β factors shown in (b). The β factor value has a neglectable effect on misfit change, thus nine lines overlap with each other and seem like one curve. The red dot represents λ =1.5*e^{-4} and the green dot represents λ= 5*e^{-4} .(b) The relationship of β factor vs misfit, using the smoothing factor λ=1.5e^{-4}. The red dot represents β=1.5*e^{-7} and the green dot represents β=1.5*e^{-6}.

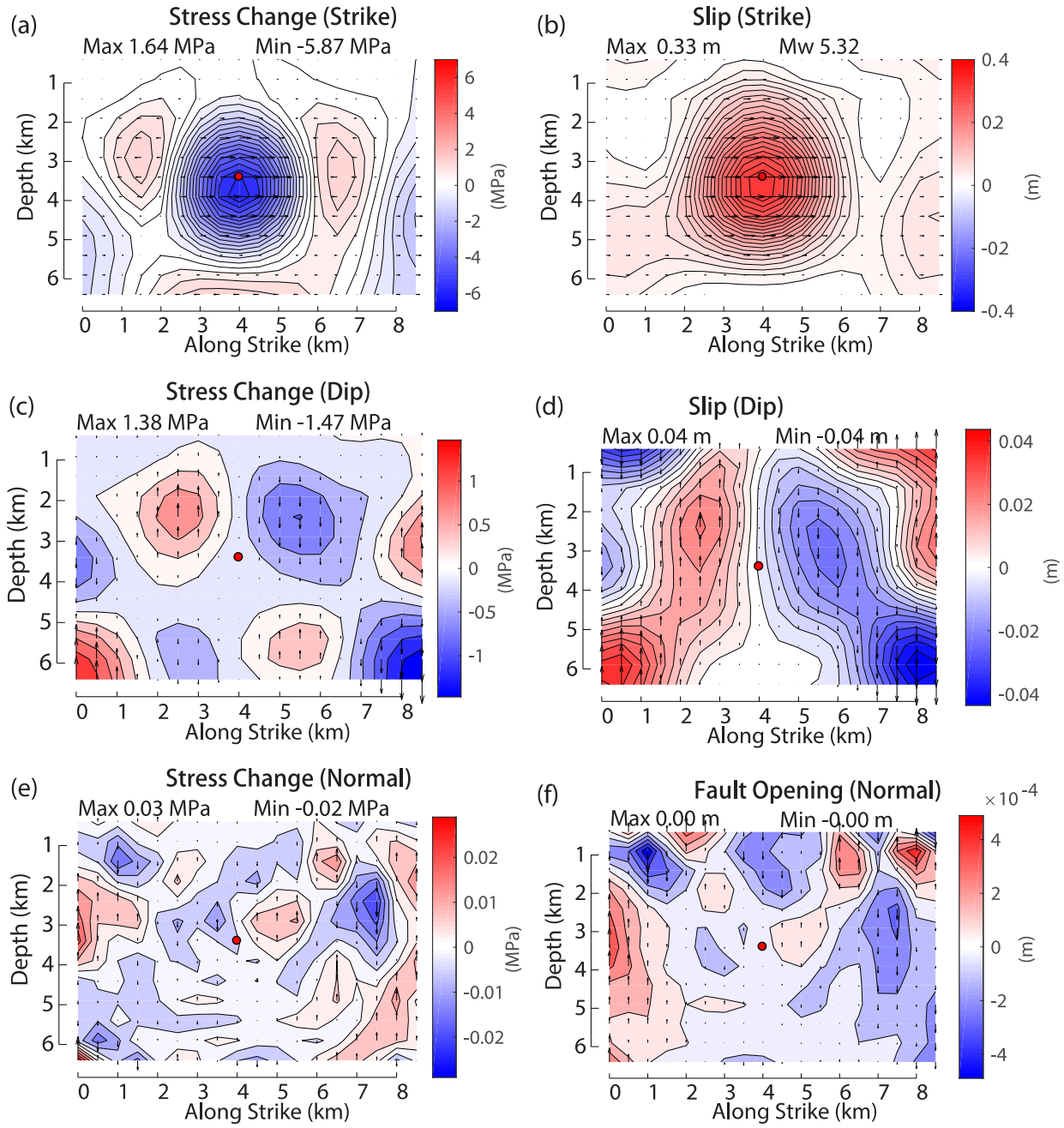

909

910 Figure 6. Inverted results INV1 for the synthetic rupture model A shown in Fig. 4, using

911 $\lambda=5e^{-4}$ and $\beta=1.5e^{-6}$ shown with green dots in Fig. 5 and using seismic data from eight

912 stations shown in Fig. 3a. (a)(c)(e) The inverted stress change on strike, dip and normal

913 directions. (b)(d)(f) The inverted slip along strike, dip and normal directions. The red dots

914 represent the hypocenter location.

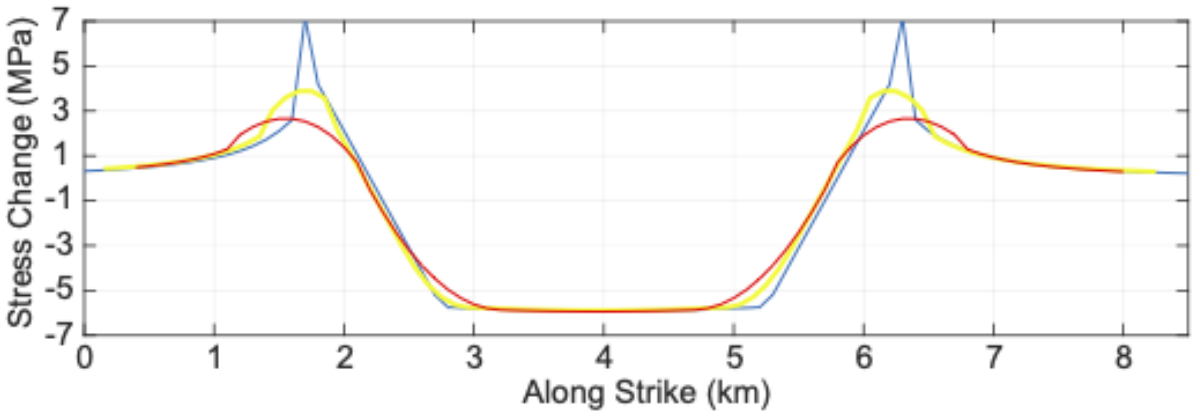

Figure 7 The stress change (blue line) along strike direction at depth of 3.5 km for the synthetic model A, shown by dashed line in Fig. 4a. The stress change is then smoothed over 500 m (one subfault) shown in yellow line and 1000 m (two subfault sizes) shown in orange line.

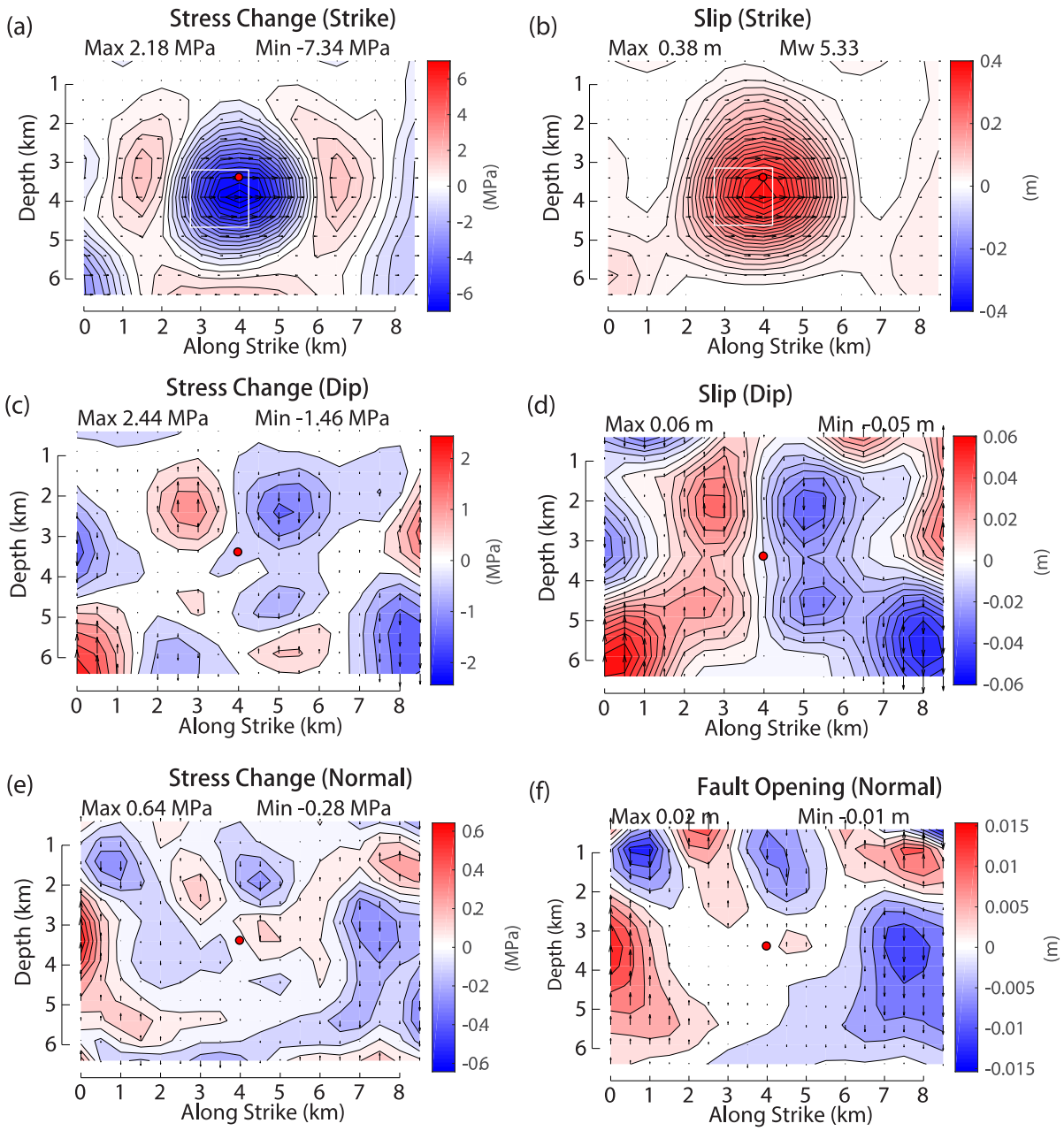

Figure 8. Inverted results INV2 for the synthetic rupture model A shown in Fig. 4, using λ=1.5e^{-4} and β =1.5e^{-7} shown with red dots in Fig. 5 and using seismic data from eight stations shown in Fig. 3a. (a)(c)(e) are inverted stress change in strike, dip and normal directions. (b)(d)(f) are associated slip along strike, dip and normal directions. The red dots represent the hypocenter location.

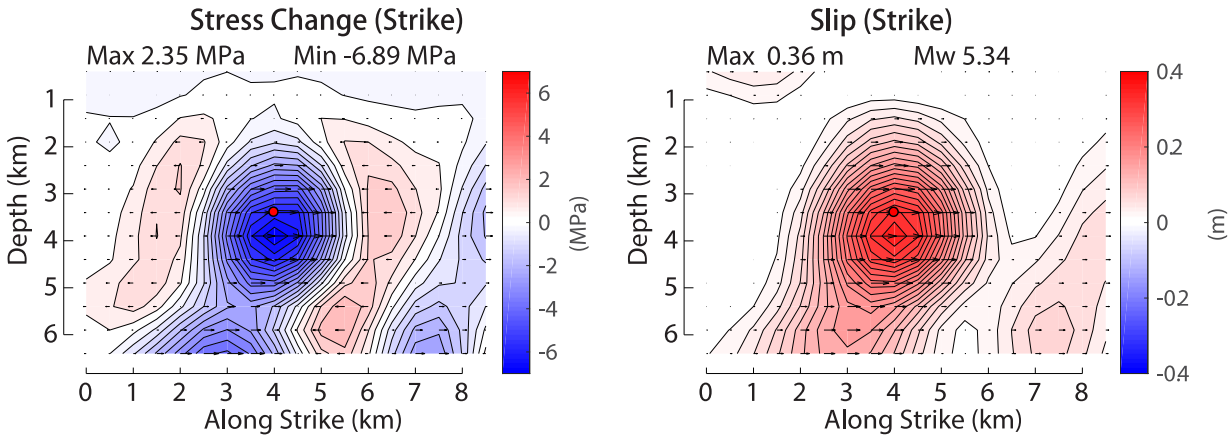

Figure 9. Inverted results INV3 for the synthetic rupture model A shown in Fig. 4, using λ=1.5e^{-4} and β =1.5e^{-7} shown with red dots in Fig. 5 and five seismic stations shown in Figure 3b. (a) is the inverted stress change in strike direction and (b) is the associated slip in strike direction.

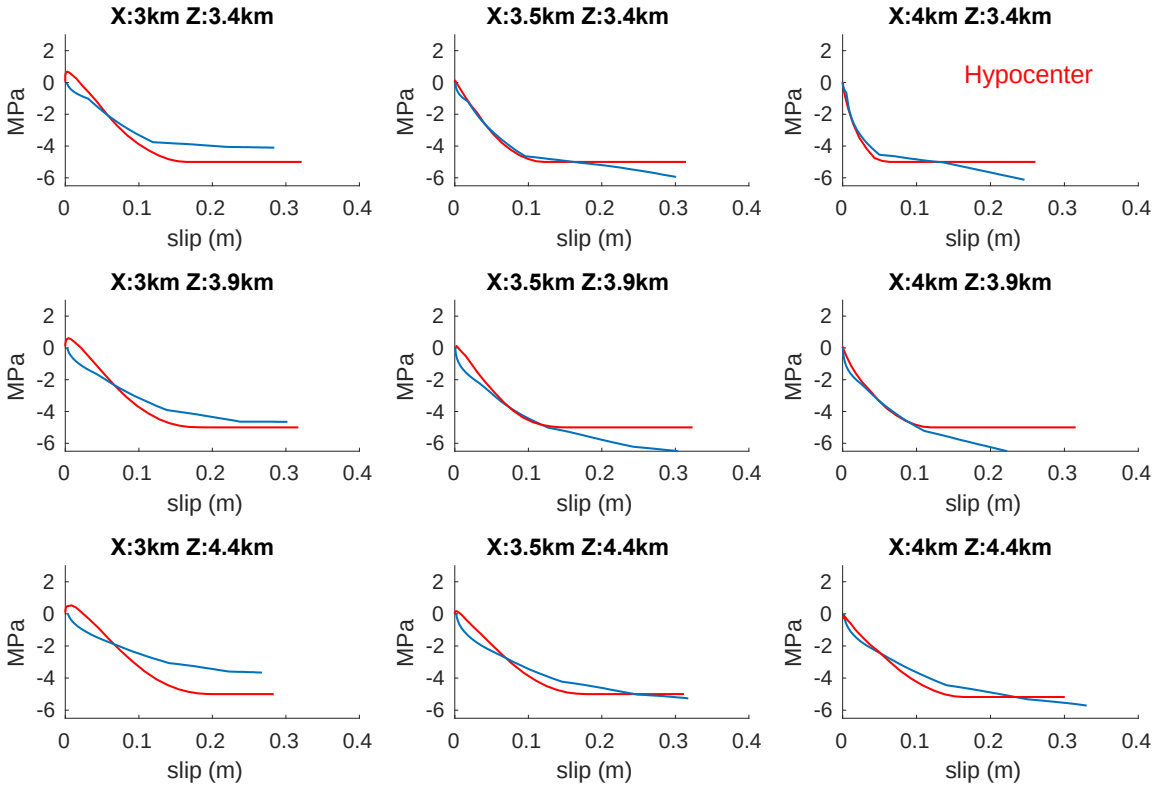

937

938 Figure 10. Slip vs stress curves for the forward model A (red lines) compared with slip vs

939 stress curves for the inverted result INV2 (blue lines), on grids located within the slip zone

940 outlined by white rectangles in Fig. 8ad. The top right panel represents slip-stress history

941 for near the hypocenter.

942

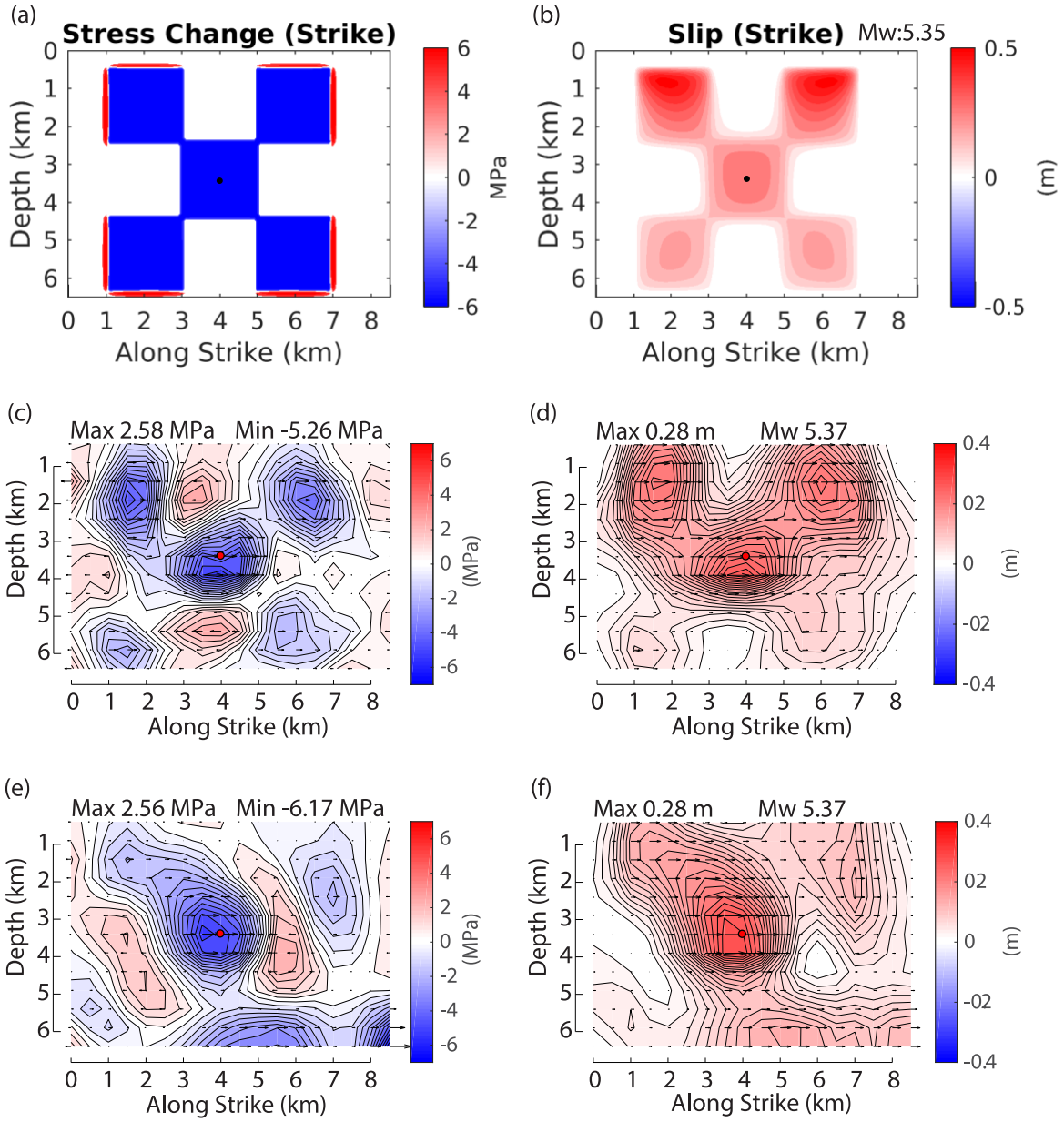

943

944 Figure 11. Checkerboard test results. (a)(b) The checkerboard model of stress changes and
945 associated fault slip along strike direction. The black dot represents the rupture initiation
946 point in the model. (c)(d) The inverted result for stress changes and fault slip along strike
947 direction, using eight stations for inversion as shown in Fig. 3a. (e)(f) The inverted result
948 for stress changes and fault slip along strike direction, using five stations for inversion as
949 shown in Fig. 3b.

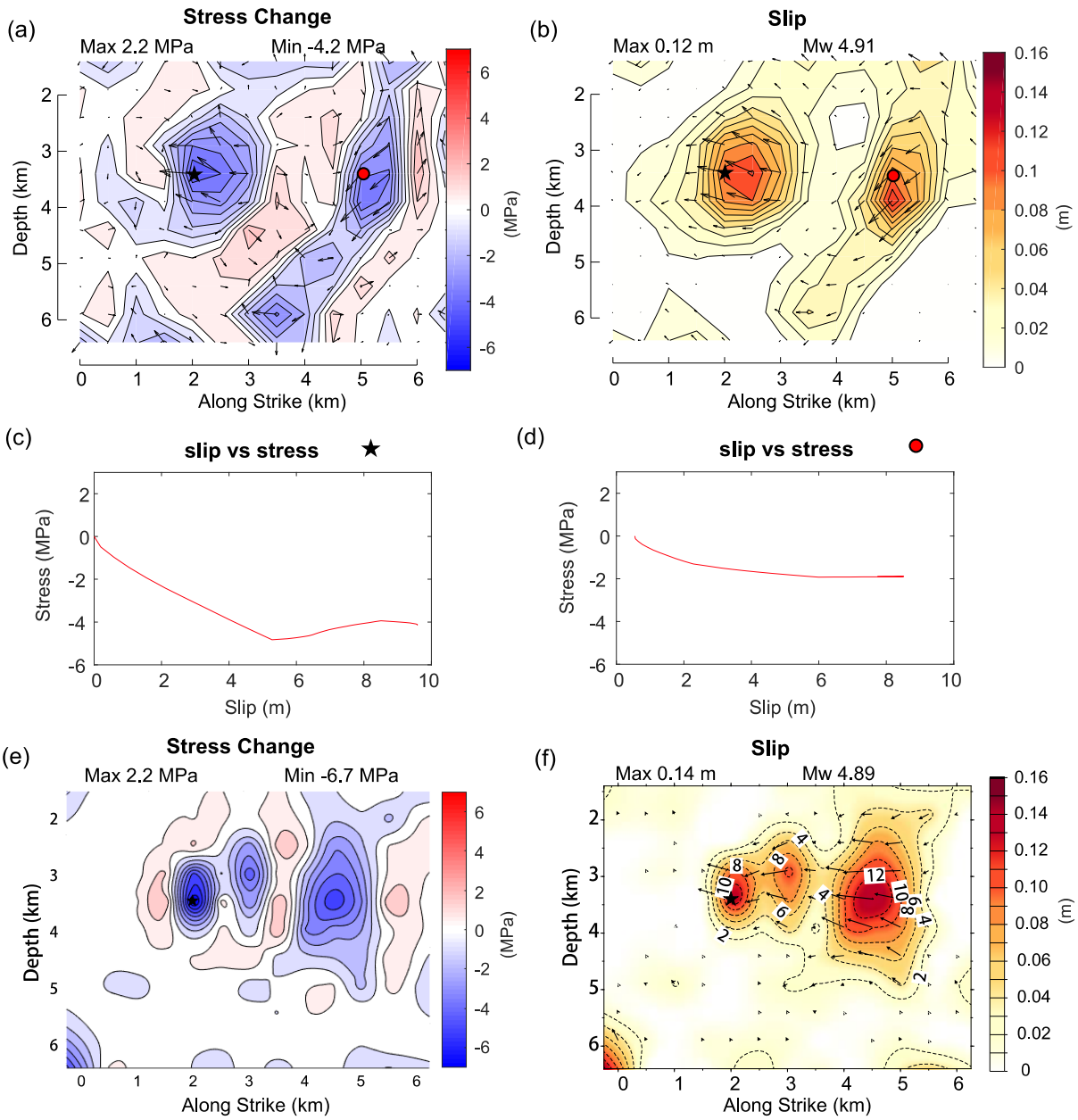

Figure 12. Comparison of the inverted stress change (a)(e) and resultant final slip (b)(f) between the dynamic stress inversion method (top) the kinematic slip inversion method (bottom). Slip-stress evolution history for the hypocenter (central point of the left slip patch in (a)) is shown in (c) and for the central point in another slip patch in (a) is shown in (d).